Metallurgy and Mechanics of Plasticity-Induced
Damage Evolution and Fracture

ISIJ International, Vol. 66 (2026), No. 4, pp. 525–533
https://doi.org/10.2355/isijinternational.ISIJINT-2025-325

A Detailed Evaluation on Plastic Deformation Mechanisms of Lath Martensite in Low-carbon Steel Using High-resolution Digital Image Correlation

Sien LIU,1)* Karel BLANKEN,1) Jiaqiang DANG,1) Fabien BRIFFOD,2) Wujun YIN1,3) and
Shoichi NAMBU1)*

1) Department of Materials Engineering, Graduate School of Engineering, The University of Tokyo, 7-3-1, Hongo, Bunkyo-ku, Tokyo, 113-8656 Japan.
2) Research Center for Structural Materials, National Institute for Materials Science, 1-2-1 Sengen, Tsukuba, Ibaraki, 305-0047 Japan.
3) Department of Materials Science and Engineering, Kyoto University, Yoshida Honmachi, Sakyo-ku, Kyoto, 606-8501 Japan.

(*Received September 29, 2025; Accepted November 18, 2025; Advance online published November 27, 2025; Published March 30, 2026*)

We employed the high-resolution digital image correlation study to investigate the plastic deformation of low-carbon lath martensite. The strain localization bands were mainly categorized into two types: boundary slips and intra-block deformation. Misorientation angle and inclination angle with respect to loading direction primarily determines the slip activation at boundaries. The competitive relationship between the activation of in-lath-plane and out-of-lath-plane slip systems follows the Schmid effect. The in-lath-plane slip systems were only activated in blocks with high in-lath Schmid factor (SF) value. The out-of-lath-plane slip systems were activated only when its SF is much higher than the maximum in-lath SF, offsetting the effect of the higher critical resolved shear stress (CRSS) for in-lath-plane slip systems. Moreover, the block morphology also affects the slip activation behaviour: in-lath-plane slip systems in columnar blocks were preferentially activated due to both crystallographic dynamics and strain accommodation. In contrast, out-of-plane slip systems were only observed in equiaxed blocks where the boundary effect is weakened.

KEY WORDS: high-resolution digital image correlation; martensite; plastic deformation; microstructure; slip system.

1. Introduction

An optimized combination of strength and ductility is essential for advanced structural steels. Low-carbon lath martensite is widely used for its excellent strength owing to its complex substructures, high dislocation density, *etc.*1,2) On the other hand, efforts are pursued to improve the poor ductility of lath martensite, where understanding its plastic deformation behaviour is of immense significance.3)

The transformation of lath martensitic from prior austenite follows a specific crystallographic orientation which is closed to the Kurdjumov-Sachs (K-S) relationship ($\{110\}_{\alpha'} \| \{111\}_{\gamma}$, $<1\bar{1}1>_{\alpha'} \| <1\bar{1}0>_{\gamma}$).4) This provides 24 crystallographic variants (4 habit-plain and 6 direction variants). Within a prior austenite grain (PAG), lath martensite typically exhibits hierarchical substructures: packets, blocks and laths.5) Upon external loading, the plastic deformation of lath martensite is accomplished by two types: intra-block slips6) and boundary sliding due to dislocation pile-ups.7,8) Both types are attributed to the crystallographic and morphological constraints in the lath martensite.

Intra-block slips can be activated along different crystallographic active slip systems, which are $\{110\}<111>$ and $\{211\}<111>$ in bcc lattice structure. The slip systems can be classified into two types: those along the habit plane are named in-lath-plane slip systems, and other active slips not along the habit plane are named out-of-lath-plane slip systems.9) Michiuchi *et al.*10) and Nambu *et al.*11) conducted a crystallographic analysis and revealed that the in-lath-plane slip systems are preferentially activated in tensile deformation. Micro-tensile tests7,12) showed that critical resolved shear stress (CRSS) for in-lath-plane slip systems are relatively lower, attributed to the boundary impeding effect on out-of-lath-plane slips. Ishimoto *et al.*13) showed that the anisotropic deformation of lath martensite arises from the

---

* Corresponding author: E-mail: sien_liu@metall.t.u-tokyo.ac.jp (S. Liu)
nambu@metall.t.u-tokyo.ac.jp (S. Nambu)

interaction between dislocation glide and lath boundaries, and consequent slip system selection.

So far, studies have been attended to explain intra-block deformation mechanisms by Schmid effect and block boundary's impeding effect. At sub-micron scale, Harjo *et al.*[14] found that dislocations can easily move, accumulate and annihilate, leading to partitioning effect between in- and out-of-lath-plane slip systems. Gong *et al.*[15] employed *in-situ* tensile electron channeling contrast imaging (ECCI) observation and suggested that the activation of slip system is dominated by Schmid factor (SF) only. Meanwhile, many studies suggested that boundary effect plays an important role. Yoshida *et al.*[16] found that block size affects intra-block dislocation recovery and movement. It is also reported that effective block size can influence the activation of slip systems, following a Hall-Petch like relationship.[17,18] However, studies at different scales show controversy on slip system activation, especially for the out-of-lath-plane slips. This is due to the lack of experimental techniques which can precisely correlate the deformation behaviour with crystallographic features.

For the plasticity at substructural boundaries, Koga *et al.*[19] performed a replica digital image correlation (DIC) analysis and found that high-strain regions primarily occur along prior austenite grain boundaries (PAGBs) and packet boundaries. Morsdorf *et al.*[5] conducted a DIC study and indicated that boundary sliding is preferentially activated with near 45° orientation respect to the loading direction. subsequent boundary sliding. On the other hand, the interaction with dislocation and block boundary is still unclear. Ueki *et al.*[20] indicated that in-lath-plane dislocations gliding can transfer across the low-angle grain boundaries (LAGBs) within blocks. Further understandings were limited by the characterization method on plastic deformation with respect to the hierarchical microstructure.

As a solution, recent development of the high-resolution digital image correlation (HR-DIC) technique improves the resolution into nm-scale.[21] This enables an accurate correlation between martensite substructure and local deformation mechanisms. In this study, we employed the HR-DIC technique to. It is aimed to clarify the criteria of slip activation, both in-lath and out-of-lath systems, as well as the effect of grain morphology.

2. Experimental Procedure

2.1. Tensile Specimen

In this study, a two-layer martensite/austenite tensile specimen was designed to improve the ductility of the lath martensite. A 0.2C low-carbon steel (Fe-0.2%C-3%Mn, wt.%) with 0.5-mm thickness was used for the martensite layer, and a SUS304 stainless steel (Fe-0.04%C-0.53%Si-0.92Mn-8.07Ni-18.19Cr, wt.%) with 1-mm thickness was employed for the ductile austenite layer. Both the 0.2C steel and SUS304 plates were homogenized at 1 423 K for 10.8 ks, and then cut into double dog-bone tensile specimens with the same gauge dimension of 10×3.2 mm (**Fig. 1**(a)). The 0.2C steel tensile specimens were subjected to austenitization at 1 323 K for 0.6 ks and water quenching to 293 K for achieving a full martensite microstructure. Finally, one piece of 0.2C steel specimen and one SUS304 specimen were bonded by alpha-cyanoacrylate adhesive, forming a 1.5-mm two-layer tensile specimen.[22] Previous studies showed that the ductile austenite layer will not induce local plasticity accommodation in the martensite layer, where a uniform deformation of martensite can be expected.[23]

Uniaxial tensile was conducted at an engineering strain rate of 1×10^{-3} s^{-1} (AGX-V2, Shimadzu). *In-situ* observation (digital microscope VHX-1000, Keyence) was conducted to capture the strain by using the MATLAB video labeler algorithm (Image Processing Toolbox).[24]

2.2. HR-DIC Methodology

The observing surface of the martensitic 0.2C steel specimen was polished using SiC abrasive papers, 1-μm alumina solution and 0.04-μm colloidal silica solution. EBSD analysis (accelerating voltage: 15kV, step size: 80 nm, JSM-7200F,

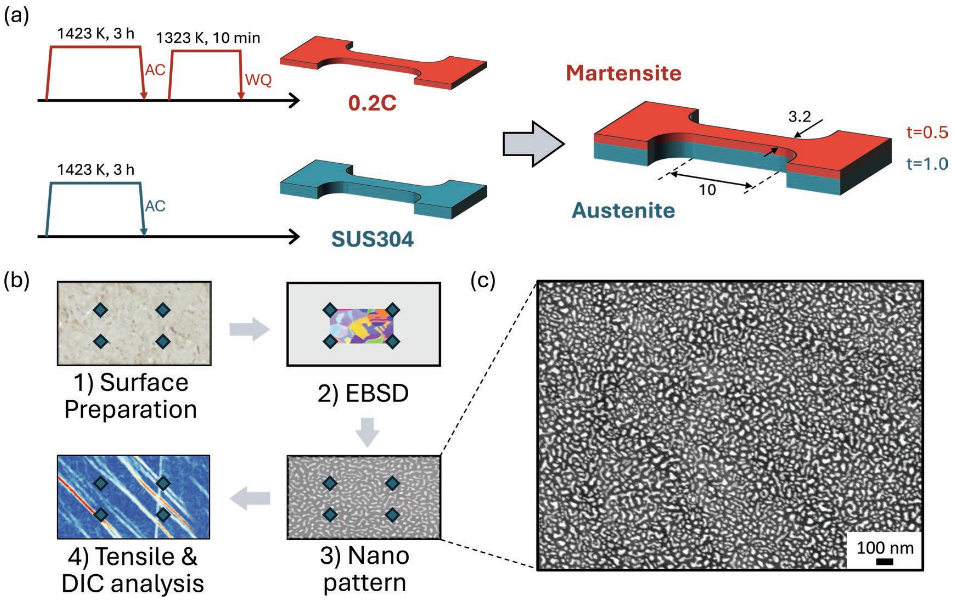

Fig. 1. Sample preparation procedures of the specimens. (a) the fabrication process of the two-layer specimens. (b) the preparation procedures for both EBSD and HR-DIC analyses. (c) an example of the nano pattern used for DIC characterization. The average pattern size is about 20 nm.

JEOL) was performed to characterize the initial microstructure. Then the DIC nano patterns were constructed by remodeling 5-nm Au layer sputtered on the observing surface using water vapors.[21] An average pattern size of about 30 nm has been achieved, as shown in Fig. 1(b).

The DIC patterns were tracked to indicate the in-plane plastic deformation strains. Backscattered electron images (BSE, accelerating voltage: 15 kV, probe current: 8 nA, JSM-7900F, JEOL) with uniform ×7 000 magnification were captured before and after the deformation. For each capture, a region of interest (ROI) of 150×150 μm was scanned by a mosaic of 11×15 images, where each image has a size of $1\,280\times960$ pixels (spatial resolution: 13.3 nm/pixel). The in-plane strain was calculated by using the Ncorr toolbox (subset radius:12 pixels, subset spacing: 0 pixel, strain radius 3 pixels).[25] Due to the overlapping between SEM images, straight strain patterns inevitably occurred at the edges of each image. Such overlap errors were carefully distinguished with strain localization bands.

2.3. EBSD-DIC Analysis

Parent austenite reconstruction was conducted by using the MTEX toolbox to correlate the deformation patterns with the microstructural and crystallographic features (*i.e.* hierarchical substructures, slip activities and boundary misorientations).[26] The crystallographic orientation relationship between martensite and prior austenite was defined by the 24 K–S variants, following previous studies.[1,8] By considering the variant analysis based on boundary misorientation, child grains were grouped into their likely-belonging prior austenite parent grain.[27] The detailed procedure follows the methodology in this reference.[28]

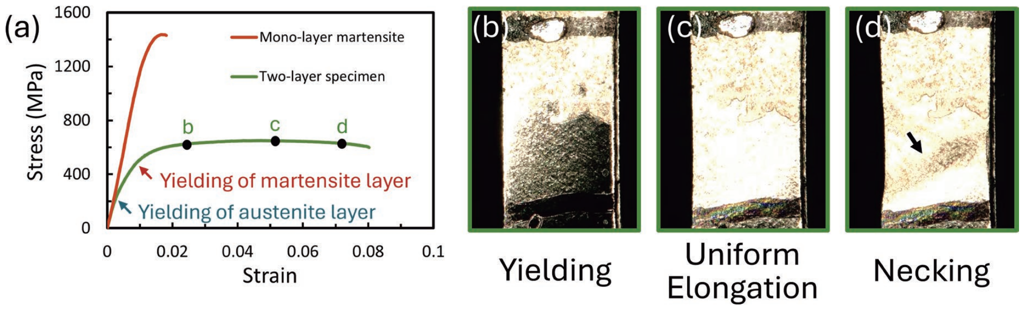

Fig. 2. (a) the uniaxial tensile test stress-strain curves of the mono-layer martensite specimen and the two-layer specimen. The overall ductility was significantly improved with employing the austenite layer. (b–d) *In situ* observations at various deformation stages during the tensile test. The three stages were selected for just after yielding, uniform elongation and before fracture, respectively.

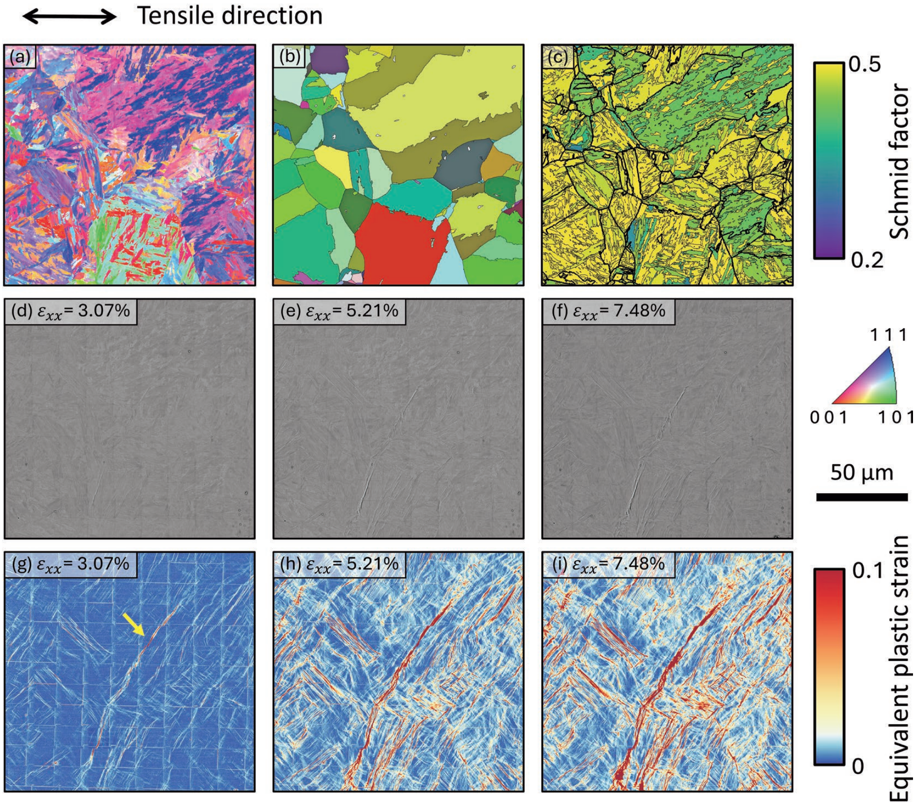

Fig. 3. The overall microstructure and DIC results of the ROI. (a) the IPF map of the ROI. (b) reconstructed parent austenite grain map. (c) maximum SF map of the ROI. (d–f) the stitched SEM images of the overall ROI at three different tensile strain values. (g–i) equivalent plastic strain maps at various stages of the tensile deformation.

The DIC strain analysis was performed using the open-source software Ncorr for MATLAB with a subset radius of 30 pixels and spacing of 1 pixel. A detailed description of the methodology was introduced in this reference.[29)]

The identification of in-lath-plane and out-of-lath-plane slip systems was implemented using the toolbox MTEX in MATLAB. In specific, the crystallographic orientation relationship between the fcc parent austenite and the bct child martensite was considering for determining the possible slip systems and respective Schmid factors. Further details are referred to this reference.[27)]

3. Results

3.1. Tensile Response

Figure 2(a) compares the stress-strain curve of the two-layer martensite/austenite specimen with that of the monolayer 0.2C lath martensite. The monolayer as-quenched lath martensite fractured prematurely at a strain of 1.8%, where the limited plastic deformation is insufficient for reliable DIC analysis. In contrast, the two-layer specimen first yielded at 193 MPa owing to the ductile layer and then yielded at 421 MPa for the martensitic layers. A uniform plastic deformation was observed by about 6%. Figures 2(b)–2(d) show the tensile response of the two-layer specimen at various stages as labelled in Fig. 2(a). Then the specimen uniformly deformed (Fig. 2(c)) and finally followed by necking as shown in Fig. 2(d). The employment of ductile layer significantly improved the tensile strain of the lath martensite.

Figure 3 presents the initial microstructure and plastic strain distribution within the ROI of the two-layer specimen. Figures 3(a) and 3(b) depict the initial IPF map and corresponding austenite reconstruction map. Figure 3(c) shows the maximum SF map considering all slip systems. To illustrate the plasticity progression, three representative strain levels were selected for exhibiting the deformation after yielding, during uniform elongation and prior to fracture. Figures 3(d)–3(f) depict the SEM observation results on the ROI at strain levels of 3.07%, 5.21% and 7.48%, where respective equivalent strain maps are shown in Figs. 3(g)–3(i). From the early stage, intense plastic strain localizes along a prominent inclined band system across the ROI (labelled by the yellow arrow in Fig. 3(g)), which progressively broadens with increasing tensile strain. This deformation band system forms an inclined angle at approximately 55° with respect to the loading direction. By superimposing with the initial microstructure, the lower part of the deformation band system is attributed to slips along PAGBs, whereas its upper part cor-

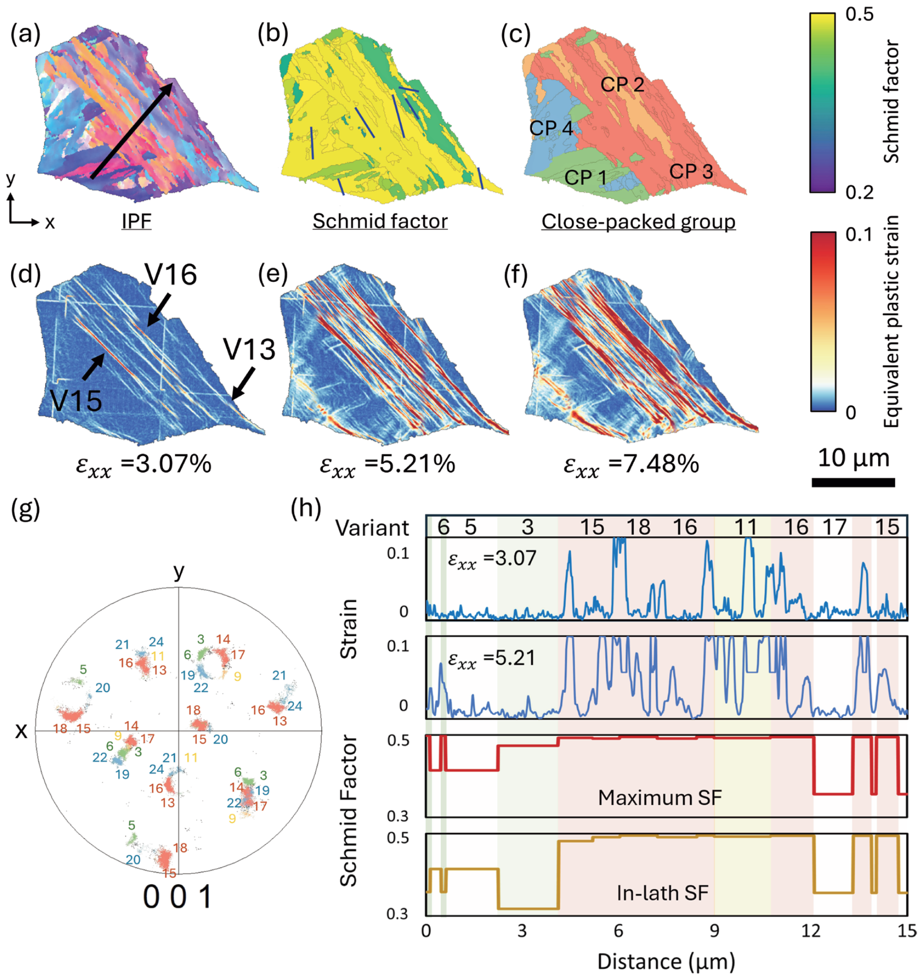

Fig. 4. A selected PAG where in-lath-plane slip systems were predominantly observed. (a) the IPF map of the selected PAG. (b) maximum SF map of the PAG. The traces of the in-lath slip planes are labelled by blue lines in some main blocks. (c) packet map of the PAG. (d–f) shows the strain maps of the PAG at various deformation stages. (g) the {001} pole figure with labels of the variants. (h) the strain profiles, maximum SF and maximum in-lath SF values of the line profile in Fig. (a).

responds to slips at substructural boundaries.

Overall, numerous strain localization bands evenly distributed in the ROI. Compared with the intense boundary-slip band system, the evenly distributed strain localization bands exhibited relatively lower strain levels, and the morphologies of the bands were strictly hindered by the substructural boundaries. As tensile strain increased, previous activated slips expended within their respective blocks, and new bands were continuously activated from other blocks. Some bands also mutually entangled with each other forming complicated strain localization systems. In the next two sections, two PAGBs are selected for analyzing their unique deformation behaviour.

3.2. Single-slip Deformation Mode

Figure 4 shows the microstructural configuration and plastic deformation of a PAG characterized by single slipping behaviour. The IPF map (Fig. 4(a)), maximum SF map (Fig. 4(b)) and close-packeted (CP) group map (Fig. 4(c)) outline the crystallographic orientation and slip activation potential within the substructures. Figures 4(d)–4(f) show progressive strain localization behaviour along specific blocks at tensile strains of 3.07%, 5.21%, and 7.48%. It can be seen that strain localization mainly occurred in the columnar grains in the same packet. Figure 4(g) displays the crystallographic orientation relationship of the variant selection in the present PAG. Notably, more strain localization bands were observed in packet 3, especially variants V13, V15 and V16. The correspondence of the microstructure with slip band morphology demonstrates that plastic deformation predominantly developed within individual blocks and impeded by surrounding boundaries.

To indicate the Schmid effect on slip activation in such single slip mode, a line profile was analyzed as labeled in Fig. 4(a). Figure 4(h) shows the strain distribution at 3.07% and 5.21% accompanying with the maximum SF values across the profile. Here, the maximum in-lath SF refers to the highest resolved shear stress (RSS) factor among all possible in-lath slip systems. In Fig. 4(h), it can be observed that all strain localization bands correspond to the block with high SF values. Notably, only the activation of in-lath-plane slip systems were observed in this PAG. Comparing the strain profile with the maximum SF values, the V3 and V6 blocks with high SF values were not activated. This is because those high SF values correspond to out-of-lath slip systems, which are not preferred in this PAG. This indicates that the CRSS or SF values are not the only factor for slip activation in lath martensite. Moreover, the maximum in-lath SF values can well predict the slip activation behaviour in V11, V15, V16 and V18 blocks. The strain localization bands were confined within each individual block, hindered by the high-angle block boundaries.

3.3. Complex Deformation Mechanisms within PAG

Figure 5 shows an example of complex plastic deformation behaviour within a PAG. Compared with those in

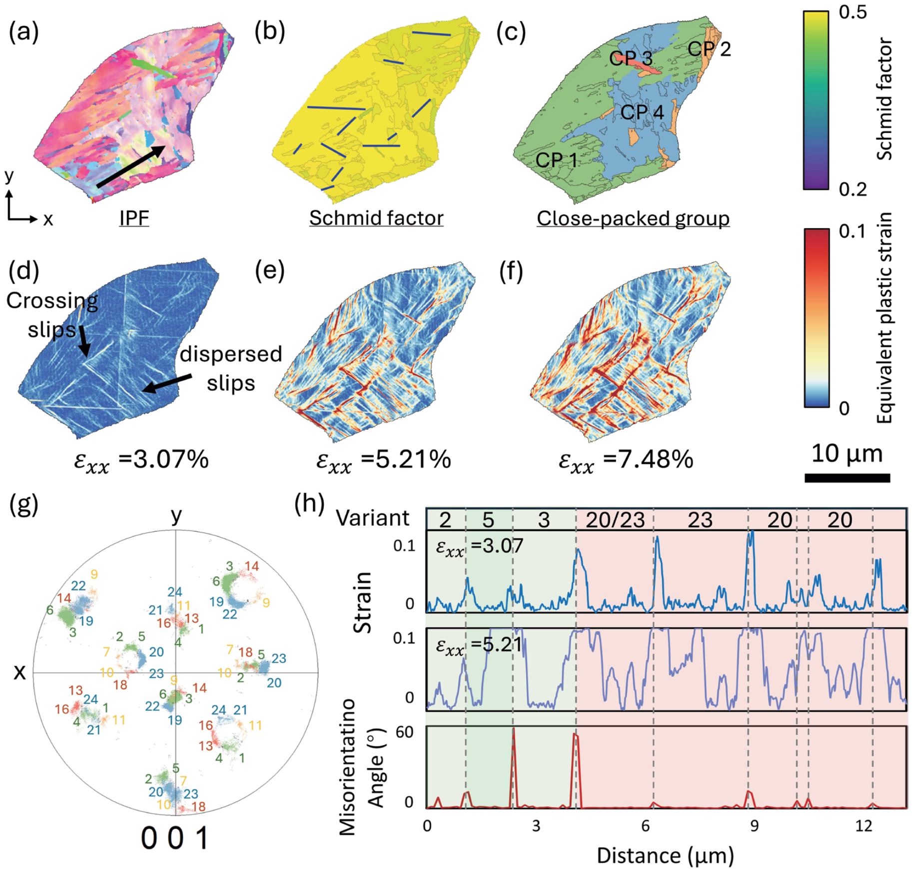

Fig. 5. A selected PAG sowing complicated deformation behaviour. (a) the IPF map of the selected PAG. (b) maximum SF map of the PAG. The traces of the in-lath slip planes are labelled by blue lines in some main blocks. (c) packet map of the PAG. (d–f) shows the strain maps of the PAG at various deformation stages. (g) the {001} pole figure with labels of the variants. (h) the strain profiles, maximum SF and point-to-point misorientation angle of the line profile in Fig. (a).

Fig. 4, the present PAG consists of more equiaxed grains and LAGBs. Figures 5(b) and 5(c) show the corresponding maximum SF map and CP group map. It can be seen that the SF values cannot explain the slip activation behaviour in this PAG. Moreover, the DIC strain maps (Figs. 5(d)–5(f)) indicate that strain localization bands exhibited in various directions, which infers a more complicated deformation mode. The strain bands were categorized into two types in terms of morphology: dispersed bands in parallel and crossing slip systems consisting of bands perpendicular to each other.

To clarify the formation mechanism of the dispersed strain localization bands, a profile analysis was conducted (profile line in Fig. 5(a)). Figure 5(h) depicts the strain localization behaviour and the misorientation angle across the profile, where a good correlation between the bands and the GB positions were observed. Moreover, peaks of strain values were observed for both high-angle and low-angle GBs. The interaction between LAGBs and dislocation gliding is complicated, exhibiting possibility of both metastable pinning and depinning effect.[30] In the PAG, the intra-block LAGBs seems to constrain the dynamics of dislocation gliding, tie the motion of dislocation lines to their respective slip planes and forms strain localization bands.[12] Since the GBs pinned the dislocations from long-term gliding, the strain bands exhibited dispersed patterns with relatively low strain values, instead of concentrated strain bands as observed in those columnar blocks (Fig. 4).

4. Discussion

In this study, the strain localization bands activation mechanisms were mainly classified into two types: boundary slips and intra-block slips. According to the strain bands, the intra-block deformation can be further categorized into two types: concentrated strain bands in columnar blocks and dispersed strain bands in equiaxed blocks. **Figure 6** depicts an example of each deformation mode, where further deformation mechanisms will be discussed in the following sections.

4.1. Boundary Slips

As observed in Figs. 3(g)–3(i), an intense strain-localization system nucleated across the ROI, exhibiting an inclination angle about 45°–60° with respect to the loading direction. This system comprises of numerous strain localization bands and exhibits highest average strain values. By correlating with the microstructure, it is confirmed that the intense strain-localization system mainly contributes to the boundary slips and activation of surrounding grains. Figure 6(a) depicts a section of the strain-localization system. The deformation bands followed the PAGB in the lower left part. Upon reaching the PAGB junction, the boundary slip bands tended to propagate along the block boundaries with similar inclination angle, instead of other PAGBs with greater rotations. This suggests that boundary slipping behaviour is influenced by local boundary characteristics: misorientation angle and inclination angle.

To clarify the activation criteria of boundary slips, **Fig. 7**(a) shows the distribution of overall and slipped boundaries in terms of misorientation angle, focusing on only HAGBs. While the trends of overall and slipped boundaries are similar, the activation of boundary slips mainly occur at HAGBs, regardless of whether they are PAGBs, packet or block boundaries.[6] Figure 7(b) shows the effect of inclination angle, which represents the relationship between boundary's crystallographic orientation and loading axis. The length frequency of slipped boundaries is mainly concentrated between 40°–65°. The region slightly deviates from the 45°[5] possibly because of the limited ROI sample size. Additionally, the distribution of strain contribution indicates that the high-strain bands concentrate at those boundaries with inclination angles between 45°–60°, whereas the low- and high-inclination-angle boundaries contributed little to the overall plastic deformation.

It is noteworthy that the boundary slips observed in this study include both the sliding along the boundaries and deformation in surrounding blocks. Figure 6(a) shows an example where severe strain localization bands were first observed along the PAGB and block boundaries, and then induced further deformation in surrounding blocks. Slip activation in these blocks exhibited non-Schmid effect, where the activated blocks are independent to their Schmid factor values. The directions of these strain localization bands are hardly constrained by the crystallographic resolved shear stress, but rather tends to be parallel to the nearby boundary slip directions. This indicates that slip activation in these grains are dominated by local dislocations, differing from the orientation-dominant slip activation in common blocks.[31] Similar geometrically necessary deformation was also reported at martensite/austenite boundaries for accommodating shape strain with dislocation gradient.[32]

4.2. Activation of Out-of-lath-plane Intra-block Slips

Although the activation of in-lath-plane intra-block slips can be well predict by the maximum in-lath SF,[9] while the out-of-lath-plane slipping mechanism and its contribution to overall deformation strain are still unclear. **Figure 8** shows an example of a block in which strain localization bands predominantly develop along out-of-lath-plane slip system. In this block, the maximum SF value is 0.493 along the red line direction in the {112} pole figure, and the maximum in-lath SF value is 0.377 following the green line in the {110} pole figure. Under tensile loading, the strain localization bands first nucleated along the {112} out-of-lath plane, as shown in Fig. 8(c). With further deformation, intense strain localization bands were mainly observed along the maximum-SF out-of-lath plane, while in-lath-plane slip systems also activated as shown in Fig. 8(f).

The results confirm that the activation of out-of-lath-plane slip systems follows the Schmid effect: the dynamic potential for out-of-lath-plane slip system is more favorable by offsetting the relatively lower CRSS.[5] There exists a competitive relationship between the activation of in-lath-plane and out-of-lath-plane slip systems. In lath martensite, in-lath-plane slip systems are preferentially activated due to their relatively lower CRSS.[10,11] The slip activation for the out-of-lath-plane slip systems is dynamically constrained by the higher CRSS. When the maximum-SF plane coincides with the habit plane, the slip systems can be easily activated along the in-lath direction. Such strain bands were widely observed at the early stage of deformation. However, when the maximum-SF plane is misaligned with the habit plane, slip activation is determined by the competitive relationship between the two

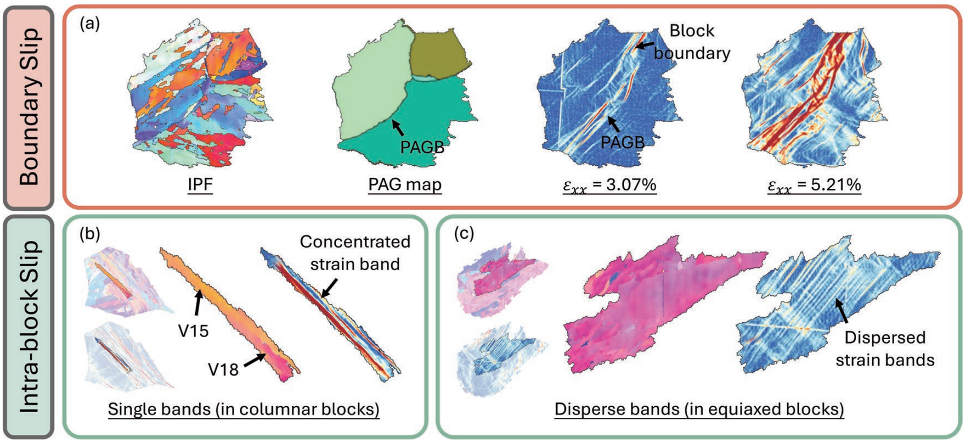

Fig. 6. The microstructure and strain maps of two deforming types: (a) boundary slip, (b, c) intra-block deformation. In this study, two types of intra-block deformation were mainly observed: (b) concentrated strain localization band and (c) dispersed strain bands.

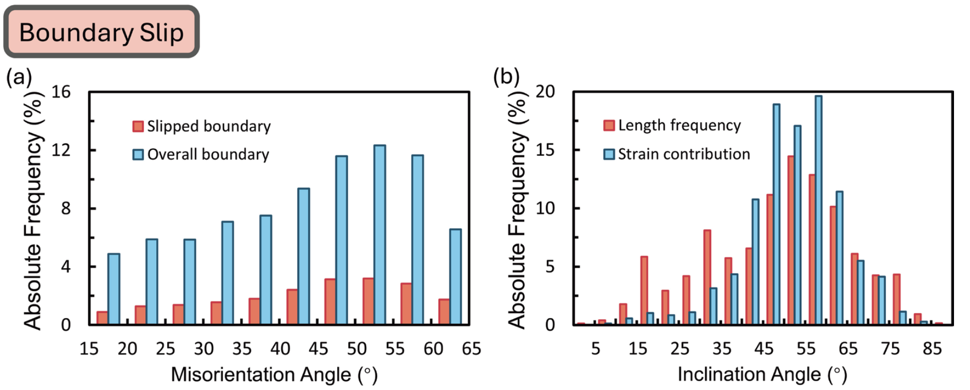

Fig. 7. (a) effect of misorientation angle on the boundary slipping behaviour. Notably, only HAGBs were analysis for boundary slipping activation. (b) effect of inclination angle with respect to loading direction on the length frequency and strain contribution of boundary slips.

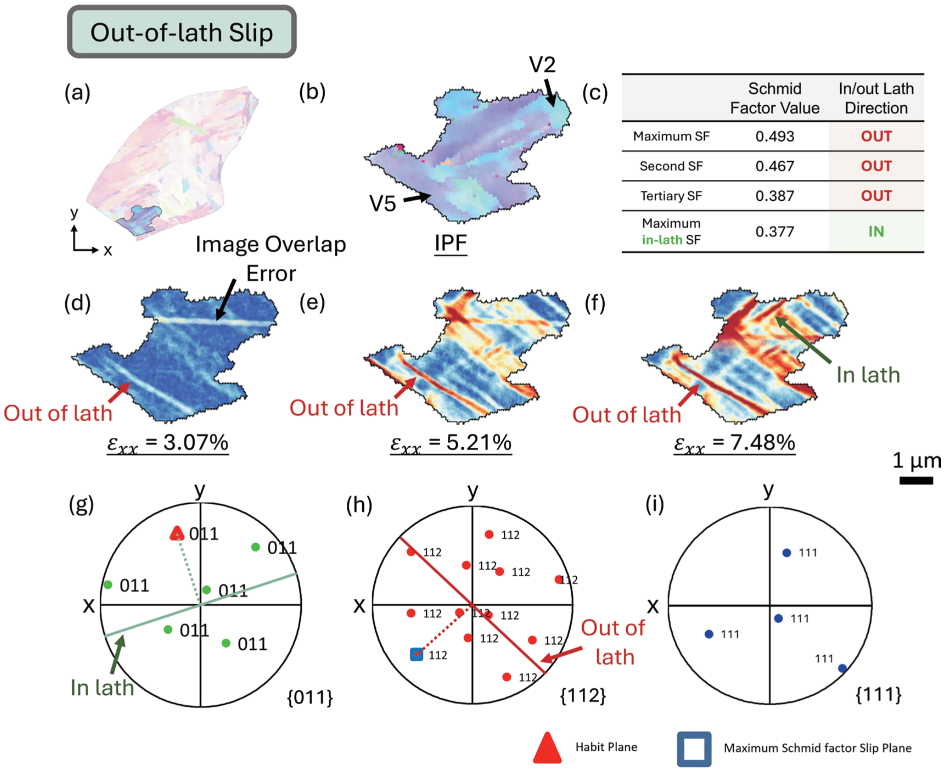

	Schmid Factor Value	In/out Lath Direction
Maximum SF	0.493	OUT
Second SF	0.467	OUT
Tertiary SF	0.387	OUT
Maximum in-lath SF	0.377	IN

Fig. 8. A selected block where out-of-lath-plane slip systems were activated. (a,c) the overall location of the block; (b) the IPF map; (c, e, f) the strain maps at various deformation stages. (g, h) the {011} and {112} pole figure with labelling the habit plane and maximum SF slip plane.

planes. In this case, the out-of-lath-plane slip systems are activated only when the SF value is high enough for dominating the dynamic potential over the CRSS difference. This explains why in-lath-plane slip systems are predominant in the deformation of lath martensite.[9] Additionally, due to the heterogeneity of stress distribution within blocks, activation of both in-lath-plane and out-of-lath-plane slip systems can possibly coexist within the same block.

4.3. Intra-block Deformation Mechanisms

Figures 9(a) and 9(b) show the effect of maximum SF and in-lath SF in the slip activation behaviour in effective blocks. Activation of both in-lath-plane and out-of-lath-plane slip systems were only observed in blocks with high maximum SF values. Figure 9(b) shows that maximum in-lath SF can effectively predict the in-lath-plane slip activation behaviour.[10] The activated blocks with low maximum in-lath SF values correspond to the out-of-lath-plane slip systems. This further confirms that out-of-lath-plane preferentially activates in blocks with high maximum SF values while low in-lath SF values.

Although slip activation generally follows the Schmid effect, the present results indicate that grain morphology can still introduce deviations in the slip-system activation behaviour.[24] These effects are mainly reflected in the types of slip systems activated, either in-lath or out-of-lath, and the timing of activation. Figures 6(b) and 6(c) depict two types of strain localization behaviour in columnar and equiaxed blocks: the concentrated strain localization bands mainly nucleated in columnar blocks, and the dispersed bands were only observed in equiaxed blocks.

Block morphology was further quantified by the block size and the length/width ratio. Figure 9(c) shows that large blocks are likely to deform at the early stage of tensile deformation. This is because the block boundaries behave as high-angle effective boundaries which hinder local atomic movement.[18] The observation is consistent with the Hall-Petch relationship for intra-block slip activation.[17] Figure 9(d) shows the effect of block morphology on slip system selection. Notably, in-lath-plane slip systems dominate the intra-block plastic deformation mechanism, whereas the activated out-of-lath-plane slip systems are only observed in equiaxed blocks (Fig. 8).

The localized slip behaviour in martensite blocks is determined by the interaction between activated dislocations and grain boundaries, which depends on the habit-plane orientation.[12] HAGBs hinders the dislocations gliding along all directions, whereas in-lath-plane slip systems can transfer across LAGBs.[33] In columnar blocks, dislocation gliding in the longitudinal directions is favorable for strain accommodation.[20] When the habit-pane orientation aligns with the longitudinal direction in a columnar block, the in-lath-plane slip system can be preferentially activated. In contrast, the

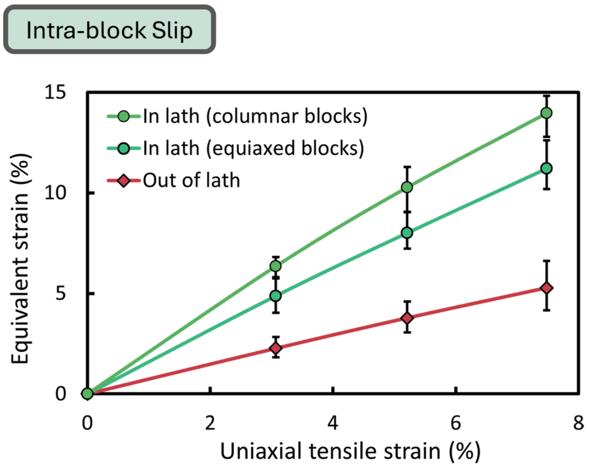

Fig. 10. Measured strain partitioning of the blocks with different slip system activation behaviour versus the overall uniaxial tensile strain.

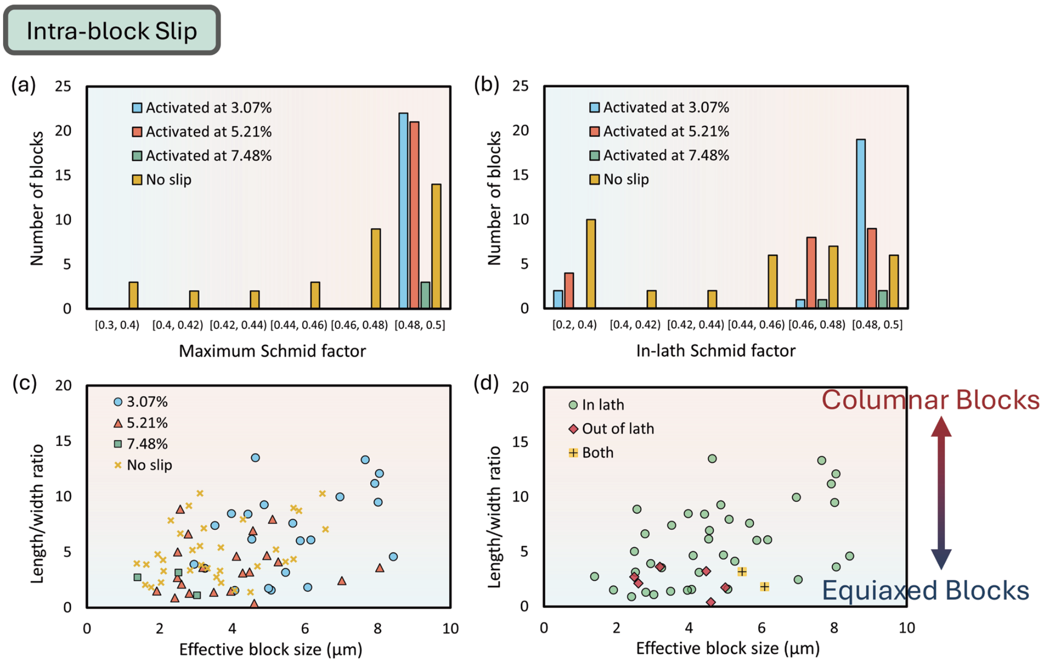

Fig. 9. Effect of (a) maximum SF and (b) maximum in-lath SF on the slip system activation behaviour for intra-block plastic deformation. (c, d) effect of block size and morphology on the slip system activation, in terms of activating strain and the types of slips.

out-of-lath-plane slip systems were strictly hindered by the block boundaries, and the slip activation is less preferred.

Briffod *et al.*[24] proposed that the intra-block plasticity arises from two components: boundary effect and bulk slipping inside blocks. In equiaxed blocks, particularly those with relatively large sizes, the boundary constraint on out-of-lath-plane slip systems is significantly reduced. Consequently, intra-block plasticity is determined by the Schmid effect in equiaxed blocks, and the out-of-lath-plane slip systems can be possible activated by the mechanisms stated in Section 4.2. This explains why the out-of-lath-plane slip systems were only observed in equiaxed blocks in this study.

Figure 10 shows the strain contributions of different intra-block plasticity types. Overall, equivalent strain developed consistently in all deformed blocks. The in-lath-plane slip systems mainly contribute to the overall plasticity of the present lath martensite, in terms of both frequency and average strain values. In contrast, out-of-lath-plane slips contribute only marginally throughout the tensile strain range. The reason is inferred that local deformation along out-of-lath planes is constrained due to the higher CRSS, compared to those along in-lath planes.[15] The LAGBs within the equiaxed blocks may also hinder the development of out-of-lath-plane slip systems, which is not observed for deformation along in-lath planes.

5. Conclusion

In this study, a high-resolution DIC (HR-DIC) technique was employed to evaluate the lath-martensite plastic deformation mechanisms in detail. A two-layer specimen effectively enhanced the overall ductility. Following conclusions are drawn.

(1) Strain localization bands can be categorized into two types: boundary slips and intra-block deformation.

(2) The activation of boundary slips is attributed to the inclination angle and boundary misorientation angle. In this study, activated boundaries concentrate at inclination angles between 40°–65° with respective to the loading direction. Boundary slips can also induce plastic deformation of surrounding blocks, which does not strictly follow the Schmid's law.

(3) Intra-block plastic deformation generally follows the Schmid effect. Maximum in-lath SF value can predict the activation of in-lath-plane slip systems. The activation of out-of-lath-plane slip systems requires two conditions: higher SF value along out-of-lath planes over the SF along in-lath planes, and weak hindering effect due to high-angle block boundary.

(4) The grain morphology influences the slip activation behaviour in martensite blocks. In columnar blocks where the habit-plane orientation coincides with the longitudinal direction, the deformation along in-lath planes are highly preferred. In contrast, deformation with out-of-lath-plane slip systems were only observed in equiaxed blocks.

Statement for Conflict of Interest

The authors declare that they have no known competing financial interests or personal relationships that could have appeared to influence the work reported in this paper.

REFERENCES

1) S. Morito, H. Tanaka, R. Konishi, T. Furuhara and T. Maki: *Acta Mater.*, **51** (2003), 1789. https://doi.org/10.1016/S1359-6454(02)00577-3
2) M. Shamsujjoha: *Materials Science and Engineering: A*, **776** (2020), 139039. https://doi.org/10.1016/j.msea.2020.139039
3) L. Morsdorf, C.C. Tasan, D. Ponge and D. Raabe: *Acta Mater.*, **95** (2015), 366. https://doi.org/10.1016/j.actamat.2015.05.023
4) H. Kitahara, R. Ueji, N. Tsuji and Y. Minamino: *Acta Mater.*, **54** (2006), 1279. https://doi.org/10.1016/j.actamat.2005.11.001
5) L. Morsdorf, O. Jeannin, D. Barbier, M. Mitsuhara, D. Raabe and C.C. Tasan: *Acta Mater.*, **121** (2016), 202. https://doi.org/10.1016/j.actamat.2016.09.006
6) C. Du, J.P.M. Hoefnagels, R. Vaes and M.G.D. Geers: *Scr. Mater.*, **120** (2016), 37. https://doi.org/10.1016/j.scriptamat.2016.04.006
7) Y. Mine, K. Hirashita, H. Takashima, M. Matsuda and K. Takashima: *Materials Science and Engineering: A*, **560** (2013), 535. https://doi.org/10.1016/j.msea.2012.09.099
8) S. Morito, H. Yoshida, T. Maki and X. Huang: *Materials Science and Engineering: A*, **438–440** (2006), 237. https://doi.org/10.1016/j.msea.2005.12.048
9) J. Inoue, A. Sadeghi and T. Koseki: *Acta Mater.*, **165** (2019), 129. https://doi.org/10.1016/j.actamat.2018.11.026
10) M. Michiuchi, S. Nambu, Y. Ishimoto, J. Inoue and T. Koseki: *Acta Mater.*, **57** (2009), 5283. https://doi.org/10.1016/j.actamat.2009.06.021
11) S. Nambu, M. Michiuchi, Y. Ishimoto, K. Asakura, J. Inoue and T. Koseki: *Scr. Mater.*, **60** (2009), 221. https://doi.org/10.1016/j.scriptamat.2008.10.007
12) S. Ueki and S. Morito: *Scr. Mater.*, **255** (2025), 116389. https://doi.org/10.1016/j.scriptamat.2024.116389
13) Y. Ishimoto, M. Michiuchi, S. Nambu, K. Asakura, J. Inoue and T. Koseki: *Journal of the Japan Institute of Metals and Materials*, **73** (2009), 720. https://doi.org/10.2320/jinstmet.73.720
14) S. Harjo, W. Gong, T. Kawasaki, S. Morooka and T. Yamashita: *ISIJ Int.*, **62** (2022), 1990. https://doi.org/10.2355/isijinternational.ISIJINT-2022-207
15) S. Gong, M. Zhang and J. Inoue: *Acta Mater.*, **280** (2024), 120337. https://doi.org/10.1016/j.actamat.2024.120337
16) S. Yoshida, Y. Arai, T. Hara and M. Kato: *ISIJ Int.*, **62** (2022), 321. https://doi.org/10.2355/isijinternational.ISIJINT-2021-469
17) K.H. Ryou, S. Nambu and T. Koseki: *Materials Science and Engineering: A*, **777** (2020), 139090. https://doi.org/10.1016/j.msea.2020.139090
18) C. Du, J.P.M. Hoefnagels, R. Vaes and M.G.D. Geers: *Scr. Mater.*, **116** (2016), 117. https://doi.org/10.1016/j.scriptamat.2016.01.043
19) N. Koga, M. Fujita, K. Shibata and S. Nanba: *ISIJ Int.*, **64** (2024), 491. https://doi.org/10.2355/isijinternational.ISIJINT-2023-121
20) S. Ueki, Y. Mine, X. Lu, Y.L. Chiu, P. Bowen and K. Takashima: *Scripta Materialia*, **203** (2021), 114045. https://doi.org/10.1016/j.scriptamat.2021.114045
21) W. Yin, F. Briffod, K. Yamazaki, T. Shiraiwa and M. Enoki: *Materials Science and Engineering: A*, **861** (2022), 144337. https://doi.org/10.1016/j.msea.2022.144337
22) S. Nambu, M. Michiuchi, J. Inoue and T. Koseki: *Composites Science and Technology*, **69** (2009), 1936. https://doi.org/10.1016/j.compscitech.2009.04.013
23) M. Ojima, A. Shiro, H. Suzuki, J. Inoue, T. Shobu, P. Xu, K. Akita, S. Nambu and T. Koseki: *Journal of the Society of Materials Science, Japan*, **66** (2017), 420. https://doi.org/10.2472/jsms.66.42010.2472/jsms.66.420
24) F. Briffod, H. Hu, T. Shiraiwa and M. Enoki: *Materials Science and Engineering: A*, **862** (2023), 144413. https://doi.org/10.1016/j.msea.2022.144413
25) J. Blaber, B. Adair and A. Antoniou: *Experimental Mechanics*, **55** (2015), 1105. https://doi.org/10.1007/s11340-015-0009-1
26) F. Niessen, T. Nyyssonen, A.A. Gazder and R. Hielscher: *J. Appl. Crystallogr.*, **55** (2022), 180. https://doi.org/10.1107/S1600576721011560
27) R. Hielscher, T. Nyyssönen, F. Niessen and A.A. Gazder: *Materialia*, **22** (2022), 101399. https://doi.org/10.1016/j.mtla.2022.101399
28) F. Briffod, T. Shiraiwa, K. Yamazaki and M. Enoki: *Materials Science and Engineering: A*, **876** (2023), 145148. https://doi.org/10.1016/j.msea.2023.145148
29) F. Bachmann, R. Hielscher and H. Schaeben: *Solid State Phenomena*, **160** (2010), 63. 10.4028/www.scientific.net/SSP.160.63
30) P. Moretti, M.C. Miguel, M. Zaiser and S. Zapperi: *Physical Review B*, **69** (2004), 214103. https://doi.org/10.1103/PhysRevB.69.214103
31) C. Hu, C. He, X. Gan, X. Wan, F. Hu, W. Zhou, H. Wang and K. Wu: *Journal of Materials Research and Technology*, **21** (2022), 5098. https://doi.org/10.1016/j.jmrt.2022.11.085
32) S. Kajiwara: *Metallurgical Transactions A*, **17** (1986), 1693. https://doi.org/10.1007/BF02817268
33) T. Ungár, S. Harjo, T. Kawasaki, Y. Tomota, G. Ribárik and Z. Shi: *Metallurgical and Materials Transactions A*, **48** (2017), 159. https://doi.org/10.1007/s11661-016-3845-4